

The Impedance Space: A Look at Mechanical Impedance Ellipses in 3D

Leonardo F. Dos Santos, Cícero Zanette, Elisa G. Vergamini, Lucca Maitan, and Thiago Boaventura

Abstract—This paper introduces a novel 3D graphical representation of mechanical impedance, named *impedance space*, to enhance the analysis of the dynamic behavior of compliant systems. This approach addresses the limitations of existing 2D graphical methods by associating the impedance control parameters with linear transformations to plot a parametric 3D ellipse, for a known oscillatory input. The well-known 2D impedance ellipses are shown to be particular projections of this 3D ellipse. Experimental results demonstrate the effectiveness of the proposed representation.

Index Terms—Impedance and force control, Interaction control, Impedance ellipses, Geometric visualisation

I. INTRODUCTION

ROBOTIC compliant actuation is paramount for safe physical interaction with unknown environments, people, or objects. Studies on muscle activation and the central nervous system have shown the concept of mechanical impedance as a representative model since the 1970s [1], [2]. Inspired by these biological principles, impedance control approaches were formally introduced a few years later, e.g. [3], offering a suitable alternative to traditional position/force control architectures for physical interaction applications. The state-of-the-art displays a broad set of implementations of interaction control based on the impedance method, ranging from machining applications to wearable robots and transparency control in teleoperation [4]–[6].

The mechanical impedance dynamics is generally designed as a mass-spring-damper. This model includes a kinetic energy-related element, the mass; a potential energy element, the spring; and a linear dissipative element, the damper. In robotics, usually, a spring-damper impedance is enough, preserving the robot’s inertia [7]. Moreover, as damping comes naturally, is not rare pure spring impedance applications [8]. Thus, impedance control dynamics is commonly depicted by 2D plots of the interaction force $f_{int}(t)$ against the deviation of the robot from its virtual equilibrium point $e(t)$ [9], [10].

The graphical representation enhances the understanding of the physical properties, including when the robot endpoint is under oscillatory input. The term stiffness ellipse is used to describe the relationship between the deviation and the forces in a task space plane, such as the x-y plane [11], [12], or just the spring forces [13]. In this context, each ellipse represents

the deviation-force relation in the x and y task directions. The term *stiffness ellipsoid* has also been coined to represent and analyze the Cartesian stiffness matrix and its dependency on the joint space configuration, as discussed in [14]. Herein, the objective is to describe the dynamics of the impedance model rather than demonstrate the relationship between stiffness or damping in different directions. Disambiguation of the word *ellipse* is highlighted here, in the context of impedance control, to clarify the difference between the concepts presented here and the other ellipse-based definitions.

Despite the relevance of the aforementioned methods, an explicit relationship between the parameters of the mass-spring-damper model and the graphical representation is missing. A parametric representation would be suitable for stability/passivity and performance analysis. Furthermore, it is of interest to evaluate the influence of the robot dynamics on the controller. This short paper addresses these points with the following contributions:

- a novel graphical representation of impedance on a 3D space defined by $e(t) \times \dot{e}(t) \times f_{int}(t)$, here defined as the *impedance space*. This novel representation is correlated with the standard 2D plots; of stiffness $e(t) \times f_{int}(t)$, of damping $\dot{e}(t) \times f_{int}(t)$, and of the impedance phase space $e(t) \times \dot{e}(t)$;
- a 3D elliptic curve description at the *impedance space* for a mass-spring-damper impedance under a sinusoidal input. From a 2D unity radius circle and linear transformations, the 3D elliptic curve is parameterized by the model mass, stiffness, and damping.
- an experimental evaluation of the 3D elliptic curve by constructing the impedance space from real data and an ellipse fitting for parametric evaluation.

Herein, the focus is solely on active compliant control through the impedance analogy or similar compliant control topologies applicable to torque-controlled robots. However, the proposed method can be extended to admittance control, physical interaction control, or any other model-based method. The rest of this paper is structured as follows: Sec. II introduces relevant concepts, the impedance dynamic model, and the 2D graphs for stiffness and damping visualization for a sinusoidal input; Sec. III derives the parametric equation of the elliptic path drawn in the impedance space and demonstrates the physical reasoning of this representation for the evaluation of the impedance control; Sec. IV describes the experimental setup and tests performed to demonstrate the ellipse-based analysis; finally, Sec. V concludes this work and points out future directions.

São Paulo Research Foundation (FAPESP) supported this work under grants 2018/15472-9, 2021/09244-6, 2021/03373-9, 2023/11407-6

Authors are with the São Carlos School of Engineering, University of São Paulo, Brazil. Email: {leonardo.felipe.santos, cicero_zanette, elisa.vergamini, lucca.maitan, tboaventura}@usp.br

II. FUNDAMENTALS

Control engineers typically evaluate a control method based on its ability to track references or reject disturbances in the time or frequency domain. This assessment framework applies well to conventional robot control methods, e.g., force or position control. However, impedance control requires a different perspective. As a subset of controllers rooted in the physical domain design paradigm, impedance control functions as a dynamics-shaping tool, employing physical reasoning rather than strictly adhering to a linear time-invariant (LTI) approach [15], [16]. That is, the goal is not to track a specific position or force but to control the *dynamic* relationship between a *generalized interaction force* $f_{int}(t)$ and the deviation $e(t)$ from an *equilibrium point* x_{eq} at a designated kinematic location, referred to as the *interaction port*.

A. Impedance vs Admittance causality

The impedance and admittance causality are usually defined in terms of *effort* and *flow* [17]. Mechanically speaking, an impedance has velocity as input and force as output (as an ideal massless spring). In contrast, an admittance has force as input and velocity as an output (as an ideal infinitely rigid mass). In the Laplace domain and for a 1-DoF case, they can be defined as:

$$Z(s) = \frac{1}{Y(s)} = \frac{F_{int}(s)}{\dot{E}(s)} = \frac{F_{int}(s)}{sE(s)}, \quad (1)$$

where $Z(s)$ is the impedance, $F_{int}(s)$ the interaction force, and $E(s) = X_{eq}(s) - X(s)$ the position deviation, being $X_{eq}(s)$ the equilibrium position and $X(s)$ the current position.

As the physical interaction between two systems must be causal, i.e., one system must output what the other system expects as input, an impedance should always be coupled to an admittance, and vice-versa. For example, in situations where the robot interacts with rigid objects and environments (e.g., the floor), which tend to prefer admittance causality, the robot should behave as an impedance at the interaction port [3], [18].

B. System and error dynamics

When external disturbances are applied to the impedance-controlled system, it typically responds with the dynamics of a mass-spring-damper system defined by the parameters:

$$Z(s) = \frac{m_d s^2 + d_d s + k_d}{s}, \quad (2)$$

where m_d , d_d , and k_d are the *desired* mass, damping, and stiffness of the system.

To better analyze the resultant system, the external disturbances may be set as a periodic input to the impedance through the error dynamics:

$$E(s) = \frac{a_i s}{s^2 + \omega_i^2}, \quad (3)$$

where a_i and ω_i are the amplitude and frequency of the error input signal, respectively. The time functions are obtained from the Laplace inverse transforms:

$$e(t) = \mathbf{L}^{-1}\{E(s)\} = a_i \cos(t\omega_i), \quad (4)$$

$$f_{int}(t) = \mathbf{L}^{-1}\{Z(s)sE(s)\} = a_i (k_d \cos(t\omega_i) - d_d \omega_i \sin(t\omega_i) - m_d \omega_i^2 \cos(t\omega_i)). \quad (5)$$

C. Impedance visualization

One of the most common forms of visualizing the impedance dynamics is through 2D graphs on the planes $e(t) \times f_{int}(t)$, for stiffness, and $\dot{e}(t) \times f_{int}(t)$, for damping, as in Fig 1. In the first case, it is well known that, if only stiffness is set in the impedance controller, the dynamics is linear and given by a line with slope equals to k_d ; and, if any damping d_d is inserted in the controller, this line turns into an ellipse. The same applies to the second case, where the line slope is equal to d_d and the ellipse will appear in the case of adding a stiffness [13], [19]. Although these plots are widely used, it is not well-known that they are only 2D projections of a more complex 3D ellipse. Thus, a broader analysis is needed to better understand the impedance ellipses and their relation with the impedance parameters.

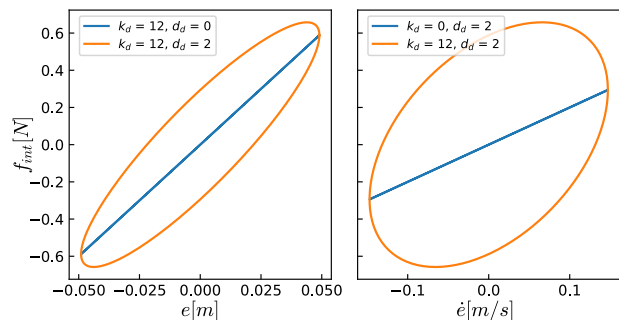


Fig. 1. Conventional 2D representation of the impedance stiffness and damping. Values of k_d in N m^{-1} and d_d in N s m^{-1} . On the left side, on the $e(t) \times f_{int}(t)$ plane, plots for a pure spring, in blue, and a spring-damper, in orange. Note how the inclination of the main axis of the ellipse changes with respect to the line. On the right side, the reciprocal on the $\dot{e}(t) \times f_{int}(t)$ plane.

III. THE IMPEDANCE SPACE

The *impedance space* encompasses three major aspects of the impedance dynamics: the stiffness plane ($e \times f_{int}$), the damping plane ($\dot{e} \times f_{int}$), and the phase plane ($e \times \dot{e}$), as shown in Fig. 2. The 3D space is defined using the *impedance states vector* $z(t)$ in an orthonormal basis as:

$$z(t) = \begin{Bmatrix} e(t) \\ \dot{e}(t) \\ f_{int}(t) \end{Bmatrix} = e(t)\mathbf{i} + \dot{e}(t)\mathbf{j} + f_{int}(t)\mathbf{k}, \quad (6)$$

where $e(t)$ and $f_{int}(t)$ are the time-dependent functions defined in (4) and (5), and \mathbf{i} , \mathbf{j} , and \mathbf{k} are the basis vectors on the x , y , and z axes, respectively. The 3D impedance space allows the generalization of the typical 2D representations as projections into specific planes, as depicted in Fig. 2. The impedance states vector $z(t)$ could also be defined with four states to include the error acceleration \ddot{e} . This would add a fourth dimension to the *impedance space* and a new 2D projection plane $\ddot{e} \times f_{int}$.

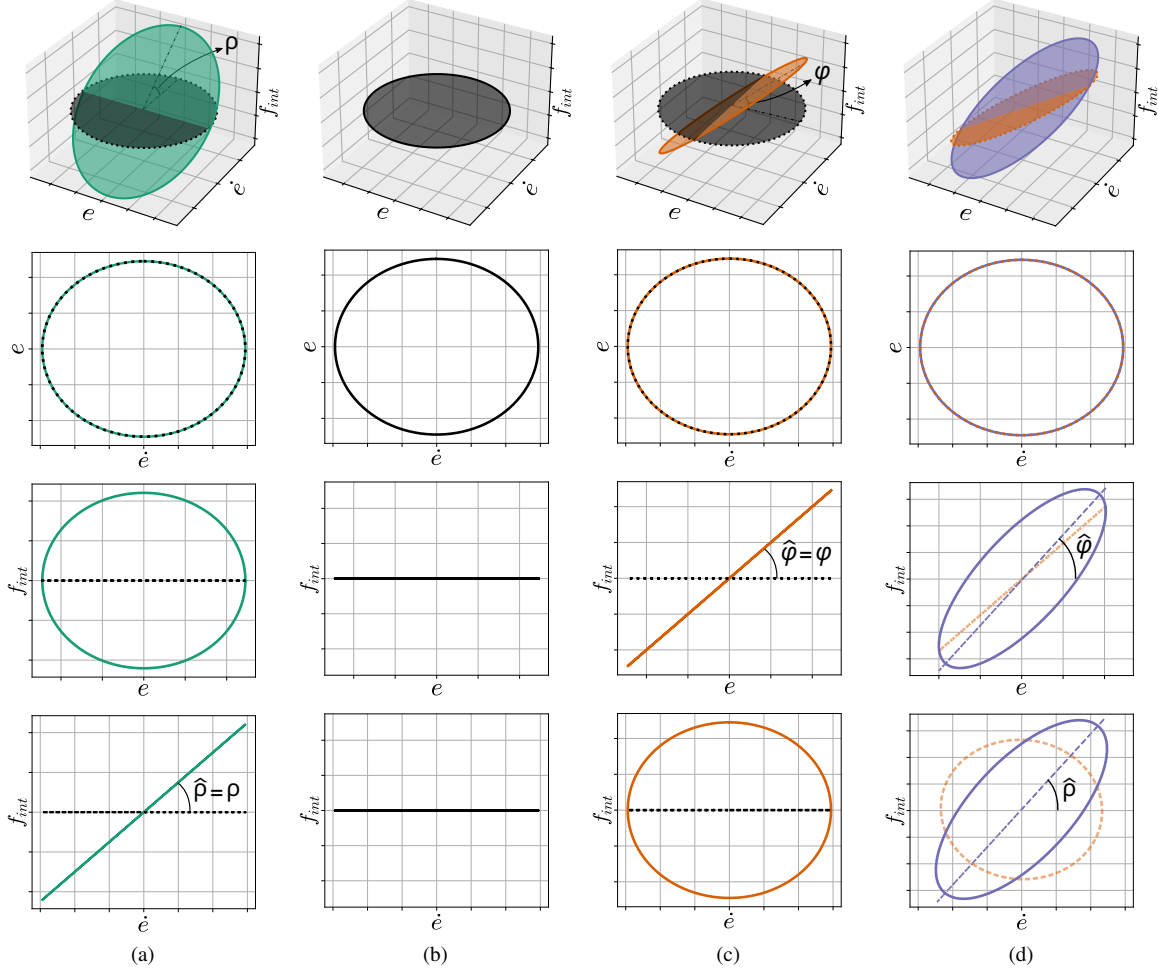


Fig. 2. Visualization of the theoretical impedance plots. Each column represents a specific combination of impedance parameters k_d and d_d ($m_d = 0$ for all of them), while the rows show different views of the impedance plot for each case. The first row, in particular, shows the 3D *impedance space*. In (b), where $k_d = 0$ and $d_d = 0$, only the original unit circle is plotted, from which the other columns derive. In (a), $d_d \neq 0$ is added, and the original circle, in black, is elongated and then rotated by ρ around the e axis. An ellipse appears in the 3D plot, with a projection on the plane $\dot{e} \times f_{int}$ being a straight line with the slope given by $\tan(\hat{\rho}) = \tan(\rho) = d_d$. In (c), $k_d \neq 0$ is added to the original circle in (b), which is elongated and then rotated by φ around the \dot{e} axis in this case. The 2D ellipse projection on $e \times f_{int}$ is also a straight line, with a slope given by $\tan(\hat{\varphi}) = \tan(\varphi) = k_d$. Last but not least, in (d), the original circle is transformed into a 3D ellipse with $k_d \neq 0$ and $d_d \neq 0$. In this case, the 2D projections in both $e \times f_{int}$ and $\dot{e} \times f_{int}$ planes are also ellipses. It is important to highlight that, for these 2D projected ellipses, $\tan(\hat{\varphi}) \neq k_d$ and $\tan(\hat{\rho}) \neq d_d$. In particular, in the $e \times f_{int}$ plane it is possible to see how the inclination changes with respect to the pure stiffness case of (c).

The dynamic system in (2) under the input in (3) describes a parametric 3D elliptic curve in the impedance space. This curve can be described by a sequence of affine transformations upon an origin-centered 2D unit circle on the phase plane, as depicted in Fig. 2b. With these transformations, the 3D elliptic curve can be derived in a time-dependent way, depending on the parameters m_d , d_d and k_d , and the input parameters a_i and ω_i , only.

To derive these transformations, the 3D ellipse can be represented using the Frenet-Serret triad: a unit vector $\mathbf{t}(t) = \dot{\mathbf{z}}(t)/\|\dot{\mathbf{z}}(t)\| \in \mathbb{R}^3$ tangent to the curve, a normal unit vector $\mathbf{n}(t) = \dot{\mathbf{t}}(t)/\|\dot{\mathbf{t}}(t)\| \in \mathbb{R}^3$ pointing to the center of the curve at t , and a binormal unit vector $\mathbf{b}(t) = \mathbf{t}(t) \times \mathbf{n}(t) \in \mathbb{R}^3$, which is orthogonal to the ellipse plane [20]:

$$\mathbf{b} = \begin{Bmatrix} b_1 \\ b_2 \\ b_3 \end{Bmatrix} = \frac{1}{\sqrt{(k_d - m_d \omega_i^2)^2 + d_d^2 + 1}} \begin{Bmatrix} k_d - m_d \omega_i^2 \\ d_d \\ -1 \end{Bmatrix}. \quad (7)$$

Projecting \mathbf{b} onto the impedance space orthogonal axes, one can derive the sequential rotation angles φ around the \dot{e} -axis, and ρ around the e -axis, in this order, as follows:

$$\tan(\varphi) = -\frac{b_1}{\sqrt{b_2^2 + b_3^2}} = \frac{m_d \omega_i^2 - k_d}{\sqrt{d_d^2 + 1}}, \quad (8)$$

$$\tan(\rho) = -\frac{b_2}{b_3} = d_d, \quad (9)$$

where the negative sign in (9) and (8) is due to the right-handed coordinate systems convention.

Before applying these two rotations, the initial 2D circle must be distorted and scaled by a transformation $\mathbf{T}_{f_{int}} \in \mathbb{R}^{3 \times 3}$:

$$\mathbf{z}(\theta) = \mathbf{T}_e(\rho)\mathbf{T}_{\dot{e}}(\varphi)\mathbf{T}_{f_{int}} \begin{Bmatrix} \cos(\theta) \\ \sin(\theta) \\ 0 \end{Bmatrix}, \quad (10)$$

where $\mathbf{z}(\theta)$ is the impedance states vector parametrized by $\theta \in [0, 2\pi]$, $\mathbf{T}_e(\rho)$, $\mathbf{T}_{\dot{e}}(\varphi) \in \mathbb{R}^{3 \times 3}$ are rotations matrices around the e and \dot{e} axes, respectively, and $\mathbf{T}_{f_{int}}$ is defined as:

$$\mathbf{T}_{f_{int}} = \begin{bmatrix} \mathbf{R} & 0 \\ 0 & 0 & 1 \end{bmatrix}, \quad (11)$$

being $\mathbf{R} = [\mathbf{f}_1 \ \mathbf{f}_2] \in \mathbb{R}^{2 \times 2}$ the basis of the conjugate ellipse diameter vectors $\mathbf{f}_1, \mathbf{f}_2 \in \mathbb{R}^2$. Using a few rotation matrix properties, \mathbf{R} may be calculated solving (10) for $\mathbf{T}_{f_{int}}$:

$$\mathbf{R} = \begin{bmatrix} a_i \sqrt{\frac{(k_d - m_d \omega_i^2)^2}{d_d^2 + 1} + 1} & 0 \\ \frac{a_i d_d (k_d - m_d \omega_i^2)}{\sqrt{d_d^2 + 1}} & -a_i \omega_i \sqrt{d_d^2 + 1} \end{bmatrix}. \quad (12)$$

Equation (10) provides a parametric expression for the second-order impedance dynamics (2) and can be used to plot the impedance ellipse in 3D.

Fig. 2 shows the isometric and perspective views of the impedance ellipse and its dependence on the impedance parameters k_d and d_d . The projection of the rotation angles ρ and φ into the $\dot{e} \times f_{int}$ and $e \times f_{int}$ planes is represented by $\hat{\rho}$ and $\hat{\varphi}$, respectively. The analytical expressions of these angle projections are very complex, highly nonlinear and dependent on all the desired impedance parameters¹. Only in particular cases, the value of these projections simplify to $\hat{\rho} = \rho$, as depicted in Fig. 2c, and $\hat{\varphi} = \varphi$, in Fig. 2a.

To better understand how the parameters influence the 2D ellipses slope, Fig. 3 and Fig. 4 show their variation when one parameter is kept constant and the other one changes.

Another interesting fact is that the impedance ellipse shape depends not only on the parameters m_d , k_d , and d_d , but also on the input amplitude a_i and frequency ω_i , as highlighted in Fig. 5. When $m_d = 0$ kg, ω_i affects only the $\mathbf{R}(2,2)$ term within $\mathbf{T}_{f_{int}}$.

IV. EXPERIMENTAL IMPEDANCE ELLIPSES

The experimental data was collected using a specially designed test bench named IC2D [21], [22], shown in Fig. 6. In both 2D and 3D, the impedance ellipse may also be plotted using experimental data to form the impedance state vector $\mathbf{z}(t)$. The inner force controller implemented in cascade with the impedance controller was a PID controller with friction compensation through disturbance observer-based control (DOB) and load velocity compensation [23], [24].

Nine separate experiments were carried out by modifying the values of the parameters k_d and d_d to illustrate how the 2D ellipses behave with different combinations of these parameters. The interaction port was manually excited, targeting a

¹The expressions can be seen in the code at https://github.com/leggedrobotics-usp/impedance_control_benchmark

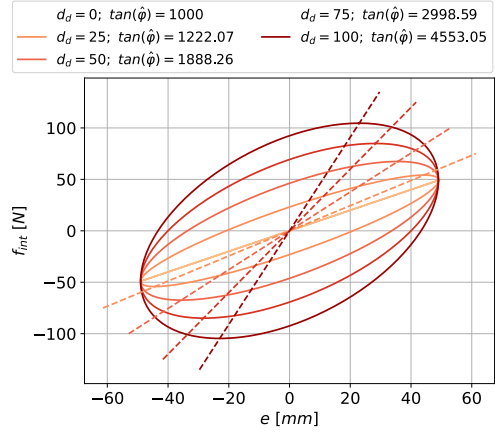


Fig. 3. Plot of the 2D projected ellipse in the $e \times f_{int}$ plane, with a fixed $k_d = 1000 \text{ N m}^{-1}$. Values of d_d in N s m^{-1} . When a damping d_d is added to the impedance controller, the slope of the ellipse major axis $\tan(\hat{\varphi})$ may significantly differ from k_d .

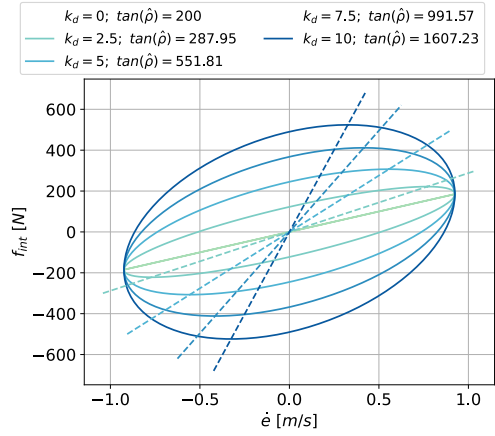


Fig. 4. Plot of the 2D projected ellipse in the $\dot{e} \times f_{int}$ plane, with a fixed $d_d = 200 \text{ N s m}^{-1}$. Values of k_d in N m^{-1} . When a stiffness k_d is added to the impedance controller, the slope of the ellipse major axis $\tan(\hat{\rho})$ may significantly differ from d_d .

sinusoidal input. Figure 7 plots the equivalent fitted ellipse for each case. The fitting technique employed was derived from the numerically stable direct least squares fitting of ellipses algorithm proposed by Halíř and Flusser [25].

A key advantage of representing the robot's impedance in a 3D space is the possibility to define new metrics to quantitatively assess the impedance emulated by the controller, comparing it with a desired parametric 3D ellipse. Some possible examples are: 1) a "interaction force fidelity" metric that measures how different the interaction force magnitudes are for each specific $\{e, \dot{e}\}$ point between the two ellipses; 2) an "impedance 3D orientation error" comparing the binormal vectors \mathbf{b} of the ellipse planes as a holistic measure taking into account both m_d , d_d , and k_d emulation; 3) parameters-specific metrics, such as a "stiffness error" and "damping error" can be directly and more easily obtained by comparing Equation 8 (for $m_d = 0$) and Equation 9, respectively, which are angles defined in the 3D space, and not in the 2D projections.

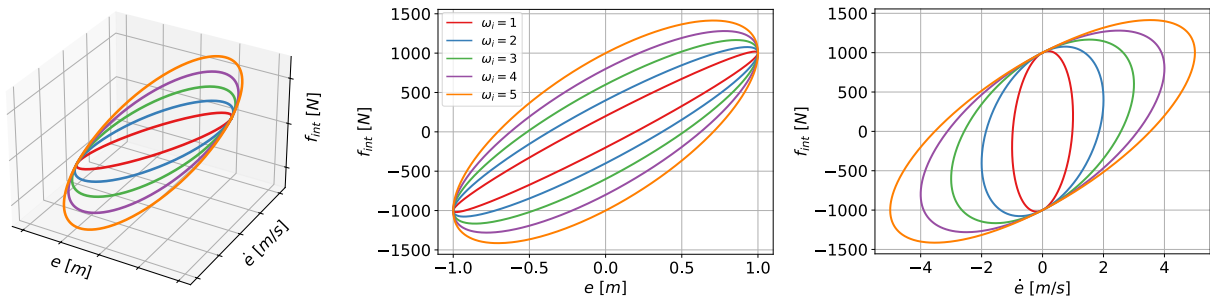


Fig. 5. Influence of the input frequency ω_i , in rad s^{-1} , on the impedance ellipses for the parameters $m_d = 0 \text{ kg}$, $k_d = 1000 \text{ N m}^{-1}$ and $d_d = 200 \text{ N s m}^{-1}$.

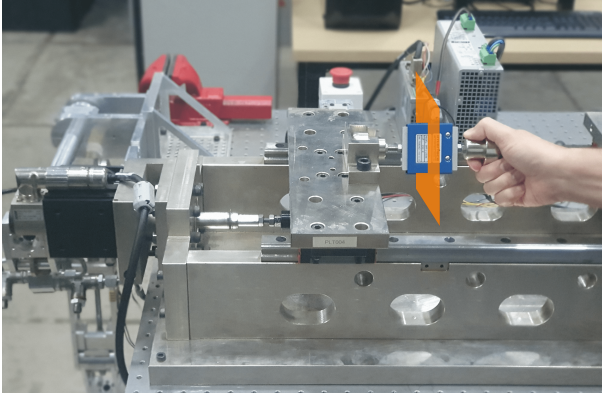


Fig. 6. Experimental setup. The interaction port is highlighted in orange. The interaction force was provided by a human hand, and a linear encoder measured the position. From left to right: linear motor, platform, load cell. The encoder is behind the platform, measuring its position.

V. CONCLUSIONS & OUTLOOK

This paper introduced and discussed a novel representation of mechanical impedance ellipses in a 3D impedance space $e(t) \times \dot{e}(t) \times f_{int}(t)$. A 3D parametric elliptical curve describes the impedance dynamics using linear transformations, which are functions not only of the impedance controller parameters m_d , k_d , and d_d , but also of the input amplitude a_i and frequency ω_i . This modeling and representation approach fosters parameter-oriented analysis of experimental time series using the designed dynamic behavior as a reference. The impedance rendering performance obtained with experimental data in this paper was limited by the inner force controller's tracking capabilities and the amplitude and frequency input fluctuations within each cycle due to the manual excitation. As a final remark, this paper highlights that the phase space $e(t) \times \dot{e}(t)$, included in the presented impedance space, supports further nonlinear and energy-based analysis. Future developments include calculating the mentioned metrics, extending the analysis including the impedance state $\ddot{e}(t)$ and the influence of inertia shaping.

ACKNOWLEDGMENTS

The authors would like to thank the Legged Robotics Group of the Robotics Laboratory of the São Carlos School of Engineering, University of São Paulo. This work is supported by São Paulo Research Foundation (FAPESP) under grants 2018/15472-9, 2021/03373-9, 2021/09244-6 and

2023/11407-6, and Brazilian Federal Agency for Support and Evaluation of Graduate Education (CAPES) under grant 88887.817139/2023-00.

REFERENCES

- [1] S. Grillner, "The role of muscle stiffness in meeting the changing postural and locomotor requirements for force development by the ankle extensors," *Acta Physiologica Scandinavica*, vol. 86, no. 1, pp. 92–108, 1972.
- [2] N. Hogan, "Tuning muscle stiffness can simplify control of natural movement," *Advances in bioengineering*, pp. 279–282, 1980.
- [3] —, "Impedance control: An approach to manipulation," *Journal of Dynamic Systems, Measurement, and Control*, vol. 107, p. 1, 1985.
- [4] Y. Huo, X. Li, X. Zhang, X. Li, and D. Sun, "Adaptive intention-driven variable impedance control for wearable robots with compliant actuators," *IEEE Transactions on Control Systems Technology*, vol. 31, no. 3, pp. 1308–1323, 2022.
- [5] M. Panzirsch, H. Singh, X. Xu, A. Dietrich, T. Hulin, E. Steinbach, and A. Albu-Schaeffer, "Enhancing the force transparency of the energy-reflection-based time-domain passivity approach," *IEEE Transactions on Control Systems Technology*, 2024.
- [6] S. Lloyd, R. A. Irani, and M. Ahmadi, "Improved accuracy and contact stability in robotic contouring with simultaneous registration and machining," *IEEE Transactions on Control Systems Technology*, 2024.
- [7] T. Boaventura, J. Buchli, C. Semini, and D. G. Caldwell, "Model-based hydraulic impedance control for dynamic robots," *IEEE Transactions on Robotics*, vol. 31, no. 6, pp. 1324–1336, 2015.
- [8] F. M. Escalante, L. F. dos Santos, Y. Moreno, A. A. Siqueira, M. H. Terra, and T. Boaventura, "Markovian transparency control of an exoskeleton robot," *IEEE Robotics and Automation Letters*, vol. 8, no. 2, pp. 544–551, 2022.
- [9] Z. Chen, N. Y. Lii, T. Wimböck, S. Fan, H. Liu, and A. Albu-Schaeffer, "Experimental analysis on spatial and cartesian impedance control for the dexterous dlr/hit ii hand," *International Journal of Robotics & Automation*, vol. 29, no. 1, pp. 1–13, 2014.
- [10] P. Song, Y. Yu, and X. Zhang, "A tutorial survey and comparison of impedance control on robotic manipulation," *Robotica*, vol. 37, no. 5, pp. 801–836, 2019.
- [11] J. M. Dolan, M. B. Friedman, and M. L. Nagurka, "Dynamic and loaded impedance components in the maintenance of human arm posture," *IEEE transactions on systems, man, and cybernetics*, vol. 23, no. 3, pp. 698–709, 1993.
- [12] M. Focchi, T. Boaventura, C. Semini, M. Frigerio, J. Buchli, and D. G. Caldwell, "Torque-control based compliant actuation of a quadruped robot," in *2012 12th IEEE international workshop on advanced motion control (AMC)*. IEEE, 2012, pp. 1–6.
- [13] S. K. Charles and N. Hogan, "Stiffness, not inertial coupling, determines path curvature of wrist motions," *Journal of neurophysiology*, vol. 107, no. 4, pp. 1230–1240, 2012.
- [14] A. Ajoudani, N. G. Tsagarakis, and A. Bicchi, "On the role of robot configuration in cartesian stiffness control," in *2015 IEEE international conference on robotics and automation (ICRA)*. IEEE, 2015, pp. 1010–1016.
- [15] A. Sharon, N. Hogan, and D. E. Hardt, "Controller design in the physical domain," *Journal of the Franklin Institute*, vol. 328, no. 5-6, pp. 697–721, 1991.
- [16] J. Lachner, F. Allmendinger, S. Stramigioli, and N. Hogan, "Shaping impedances to comply with constrained task dynamics," *IEEE Transactions on Robotics*, vol. 38, no. 5, pp. 2750–2767, 2022.

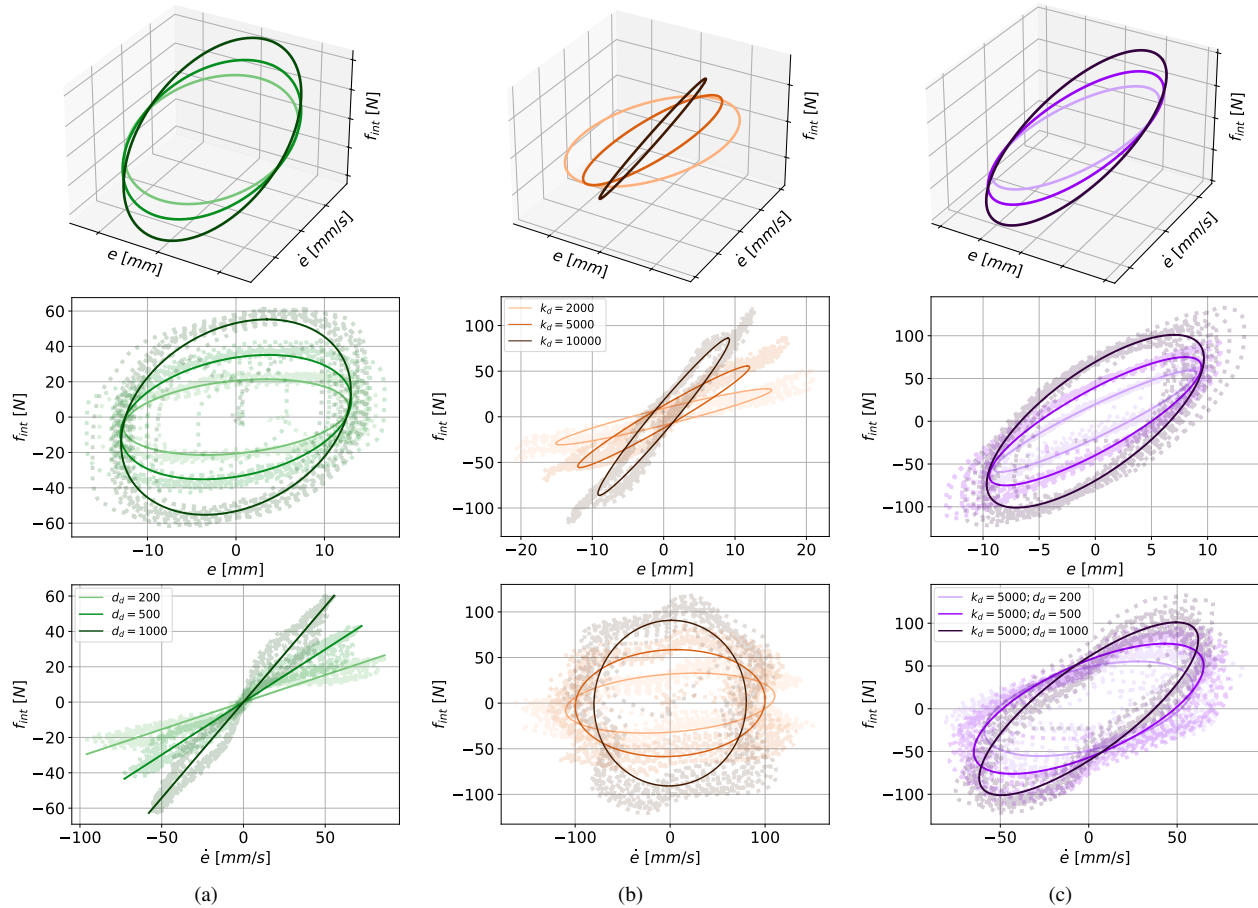


Fig. 7. Experimental results, all with $m_d = 0$ kg. (a) for $k_d = 0$ N m⁻¹ and varying the value of d_d one can see that in the $\dot{e} \times f_{int}$ plane the straight line slope increases with d_d and in the $e \times f_{int}$ plane the ellipse widens due to the projection as expected; (b) for $d_d = 0$ N s m⁻¹ and varying the value of k_d , one can see that in the $e \times f_{int}$ plane, the slope of the ellipse major axis increases with k_d and in the $\dot{e} \times f_{int}$ plane the ellipse widens due to the projection as expected. The widening of the ellipse in the $e \times f_{int}$ plane is due to unwanted damping, mostly caused by the test bench itself. As can be seen, the openings are practically the same, as the damping of the bench does not change; (c) for both parameters k_d and d_d varying, the effects combine on both planes.

- [17] N. Hogan, "Modularity and causality in physical system modeling," *Journal of dynamic systems, measurement, and control*, vol. 109, no. 4, pp. 384–391, 1987.
- [18] P. J. Gawthrop and G. P. Bevan, "Bond-graph modeling," *IEEE Control Systems Magazine*, vol. 27, no. 2, pp. 24–45, 2007.
- [19] Z. Ranko, Ángel Valera Fernández, and P. J. G. Gil, "Impact and force control with switching between mechanical impedance parameters," *IFAC Proceedings Volumes*, vol. 38, no. 1, pp. 169–174, 2005, 16th IFAC World Congress. [Online]. Available: <https://www.sciencedirect.com/science/article/pii/S1474667016373104>
- [20] J. Stewart, "Vector functions: arc length and curvature," in *Calculus: Early Transcendentals*, 6th ed. Belmont, CA: Thomson Brooks/Cole, 2008, pp. 830–838.
- [21] E. G. Vergamini, L. Felipe dos Santos, C. L. A. Zanette, Y. Moreno, F. M. Escalante Ortega, and T. Boaventura, "Construction of an impedance control test bench," in *Proceedings of the 27th International Congress of Mechanical Engineering*, ser. COB2023. ABCM, 2023. [Online]. Available: <https://www.researchgate.net/publication/378419899>
- [22] E. Vergamini, L. F. Santos, and C. Zanette, "Ic2d project," <https://github.com/leggedrobotics-usp/ic2d>, 2023.
- [23] E. Dimo and A. Calanca, "Environment aware friction observer with applications to force control benchmarking," *Actuators*, vol. 13, no. 2, 2024. [Online]. Available: <https://www.mdpi.com/2076-0825/13/2/53>
- [24] T. Boaventura, M. Focchi, M. Frigerio, J. Buchli, C. Semini, G. A. Medrano-Cerda, and D. G. Caldwell, "On the role of load motion compensation in high-performance force control," in *2012 IEEE/RSJ International Conference on Intelligent Robots and Systems*, 2012, pp. 4066–4071.
- [25] R. Halir and J. Flusser, "Numerically stable direct least squares fitting of ellipses," in *Proc. 6th International Conference in Central Europe on Computer Graphics and Visualization. WSCG*, vol. 98. Citeseer, 1998, pp. 125–132.